Published in final edited form as:
Lab Chip. 2009 January 7; 9(1): 107–114. doi:10.1039/b808660e.

Computation of transient flow rates in passive pumping micro-fluidic systems

I-Jane Chen, **Eugene C. Eckstein**, and **Ernő Lindner**
Department of Biomedical Engineering, The University of Memphis, Memphis, TN 38152, USA

I-Jane Chen: ijchen@memphis.edu; Eugene C. Eckstein: eckstein@memphis.edu; Ernő Lindner: elindner@memphis.edu

Summary

Motion in micro-channels of passive flow micro-fluidic systems can be controlled by proper design and estimated by careful modeling. We report on methods to describe the flow rate as function of time in a passive pump driven micro-fluidic systems. The model considers the surface energy present in small droplets, which prompts their shrinkage and induces flow. The droplet geometries are controlled by the micro-fluidic system geometry and hydrophilicity of the droplet channel contact area so that the chord of the droplet's cross section is restrained as the fluid is pumped. The model uses interfacial thermodynamics and the Hagen-Poiseuille equation for calculating the flow rate in micro-channels. Existing analyses consider the theoretical relationships among sample volume and induced flow rate, surface energy of the drops at the entrance and exit ports, and the resistance to flow. This model provides more specific information on the influence of the experimental conditions in computations of the flow rate. The model was validated in four sets of experiments. Passive pumps with 1.8 mm diameter, hydrophobic or hydrophilic entry ports, 5.0 or 10.0 mm channel length, and 2.5 or 3.3 mm diameter reservoir ports provided initial flow rates between 85 nL/sec and 196 nL/sec.

Introduction

Various pumping methods have been developed for use with micro-fluidic systems.[1–7] Although, these methods can provide stable flow in a wide flow-rate range, they generally require bulky equipment, which is inconsistent with the simplicity of micro-fluidic systems. Burns et. al. showed that it is possible to manipulate discrete drops inside microchannels [8, 9] for metering nanoliter volumes precisely and accurately. The integrated nanoliter DNA analysis device described by the authors worked without a conventional mechanical pump. Walker et al.[10] proposed the use of the interfacial energy in small droplets to pump liquids through micro-channels. By placing a small liquid droplet over the hydrophobic sample port of a micro-channel, fluids could be pumped semi-autonomously and semi-continuously. The mathematical model established by the authors considered the contraction of spherical droplets (pumping droplets) in a concentric pattern and utilized the Young-Laplace equation to estimate the driving force of the flow. More recently Berthier et al.[11] provided an analytical solution to describe the flow in passive pumping driven micro-fluidic devices. The applicability of the analytical solution however is limited by restrictive model assumptions.

To provide a generally applicable description of the passive pump driven flow in micro-channels, we report on numerical modeling of volume flow rate as function of time for different experimental conditions, i.e. system geometry, and the hydropobicity of the droplet-channel contact area. The model considers the surface energy present in small droplets, the hydrostatic pressure difference between input and output ports of the micro-fluidic device, and the hydrodynamic resistance of the liquid flow in a micro-fluidic channel of specified geometry. The surface energies are calculated by the original or a modified Young-Laplace equation while

the hydrodynamic resistance is assessed by the Hagen-Poiseuille equation. The model provides the induced flow rate (sample volume change over time) as a function of the driving force (overall pressure difference generated by interfacial and hydrostatic energies), hydrodynamic resistance, and time.

Passive pump

A solution-filled micro-channel with liquid droplets on its entry (sample) and exit (reservoir) ports is considered a passive pumping device when the sample fluid is spontaneously driven from the entry port to the reservoir port (Fig. 1). During the pumping process potential and interfacial energies in the sample droplet are converted into kinetic energy and heat, which are dissipated to the environment.[12] Simultaneously, the potential and interfacial energies in the reservoir droplet increase slightly.

Theory

Assumptions and mathematical model

To initiate flow in a passive pump driven micro-fluidic system, small volumes of solution are dispensed on the sample and reservoir ports of a solution-filled micro-channel, where the dispensed volumes of aqueous solutions form droplets. The shapes of the droplets are assumed to be parts of spheres. A three dimensional view of a droplet over a cylindrical well is shown schematically in Fig. 2a. Once the sample and reservoir droplets are connected, flow is generated and the size and shape of the droplets change simultaneously. At the sample port, the water/air interface is pushed inward continuously until the system achieves equilibrium and the flow stops. The changes in the shape of the sample droplet, as its volume moves into the cylindrical entry port, can be represented by cross-sectional snapshots recorded at consecutive time instances, t_i, t_{i+1}, and t_{i+2}. The cross sectional snapshots shown in Figs. 2b correspond to concentric descent while the snapshots in Figs. 2c and 2d represent the pseudo-concentric descents, with decreasing or increasing droplet radii, respectively. At time instant t_0, the volume of the droplet is the largest, and its apex is the highest. The heights (h_i), the half chord length (a), and the radius (R_i) characterize the shapes of the sinking droplets. For each t_i time instant the radius (R_i), the volume (V_i), and surface area (A_i) of the droplet can be calculated:

$$R_i=(h_i^2+a^2)/2h_i \tag{1}$$

$$V_i=\pi h_i(3a^2+h_i^2)/6 \tag{2}$$

$$A_i=\pi(a^2+h_i^2) \tag{3}$$

If the contact ring (Fig. 2a) of the sample droplet remains constant as the droplet descends into the cylindrical entry port of the device, it is adequate to consider only the energy changes at the air/water interface and neglect the energy changes at the water/PDMS and air/PDMS interfaces since the areas of latter interfaces remain constant. The pseudo-concentric shapes of sample droplets, as shown during descent in Fig. 2c and 2d, are relevant examples. However, neglect of energy changes at the water/PDMS and air/PDMS interfaces cannot be justified when the area of the contact ring gradually decreases during the pumping process. The energy changes at the water/PDMS and air/PDMS interfaces can be important, during a concentric descent as shown in Fig. 2b. The patterns of sample droplet shape changes (e.g., concentric vs.

pseudo-concentric or fixed cord vs. decreasing cord) are controlled by the experimental conditions (e.g., by the *a/r* ratio), and can merge into each other during the pumping process. [11] For example, in the passive pumping device described in this paper the descent pattern of the droplet is the combination of the pseudo-concentric descents with decreasing and increasing radii. The descent starts in a pseudo-concentric fashion with gradually decreasing radius and continues in a pseudo-concentric fashion with increasing radius. In this paper we evaluate the validity of two models for calculating the passive pump driven flow rates in micro-channels. Both models are applied to experimental conditions in which the cord length of the sample droplet remains constant during the entire pumping process. These conditions are labeled as pseudo-concentric descents with decreasing or increasing radii (Figs. 2c and 2d).

Several pressure differences must be considered to compute the flow in a microfluidic channel. The one of primary concern is the pressure difference across the length of the channel, which occurs in response to the flow. This flow is induced by the shrinking sample droplet. The pressure in a droplet shrinking in concentric fashion (Fig. 2b) can be calculated with the Young-Laplace equation:

$$\Delta P_{\mathrm{i}}=2\gamma/R_{\mathrm{i}} \tag{4a}$$

However, droplets in passive pumping experiments most commonly do not shrink in a strictly concentric fashion, i.e., their centers descend while their cord length remain fixed as shown in Figs. 2c and 2d. To apply the Young-Laplace equation for these conditions, the R_{i} values in Equation 4a are calculated from the decreasing droplet volumes using Eqs. 1 and 2.

Conversely, the formula for the pressure difference for droplets is no longer a simple expression (Eq. 4b and supplementary information) if the conversion of interfacial energy E_i is calculated numerically from the changing shape of the descending droplet. An appropriate expression is:

$$\Delta P_{\mathrm{i}}=\frac{\gamma\pi(h_{\mathrm{i}}^2-h_{\mathrm{i+1}}^2)}{\int_{\theta=0}^{\theta_{\mathrm{i,max}}}2\pi R_{\mathrm{i}}^2\cdot \mathrm{d}h_{\mathrm{i,max}}\cdot\cos(\frac{\pi\theta_{\mathrm{i,j}}}{2\theta_{\mathrm{i,max}}})\cdot\sin\theta_{\mathrm{i,j}}\mathrm{d}\theta_{\mathrm{i,j}}} \tag{4b}$$

where ΔP_{i} is the pressure change in the sample droplet when its height decreases from h_{i} to $h_{\mathrm{i+1}}$, γ is the surface tension, $dh_{i,j}$ denote distances the surface points of a descending droplet travel between two time instances (Fig. 2d), ranging between $\mathrm{d}h_{i,max}$ (at the apex) and zero (at the circumference of the entry port), and $\Theta_{\mathrm{i,j}}$ are angles utilized in the numerical approximation of the descending droplet surface (see supplementary information).

Equation 4b can be considered as a modified Young-Laplace equation with rather complicated, specific expression for the radius of the droplet as a consequence of the sinking pattern. The radius of the droplet is used to calculate its surface area and volume. During the pseudo-concentric descent with decreasing and than increasing radii, the shape of the droplet above the entry port is continuously changing because as the center of the droplet sinks as it descends, the angle θ decreases concomitantly (Figs. 2c and 2d).

The overall pressure gradient ($\Delta P_{\mathrm{total}}$) in the micro-fluidic system shown in Fig. 1 is governed by the pressure differences generated at the interfaces of the sample and reservoir droplets, respectively ΔP_{S} and ΔP_{R}, and the hydrostatic pressure difference, (ΔP_{H}), due to the height difference of the liquid on the sample and reservoir sides of the micro-channel:

$$\Delta P_{\mathrm{tot}}=\Delta P_{\mathrm{S}}-\Delta P_{\mathrm{R}}+\Delta P_{\mathrm{H}} \tag{5}$$

Both ΔP_S and ΔP_R can be assessed with Eq. 4a or 4b using the appropriate droplet geometries. The ΔP_H hydrostatic pressure difference is a function of the height difference between the pumping (sample) and reservoir droplets. ΔP_H changes simultaneously with the decrease of the sample and increase of the reservoir droplet volumes. At time instant t_i the hydrostatic pressure difference can be expressed as:

$$\Delta P_{H}=\rho g(h_S - h_R) \tag{6}$$

where ρ is the density of the liquid, g is gravitational constant, while h_S and h_R are the heights of the apexes (indeed the heights of the centers of gravity) of the sample and reservoir droplets, respectively.

The flow rate (Q_i) in a passive flow driven micro-fluidic device, can be calculated from the overall pressure gradient (ΔP_{total}) across the flow path and the hydrodynamic resistance (Ω) of the micro-channel:

$$Q_i=\frac{\Delta V_i}{\Delta t_i}=\frac{\Delta P_{tot}}{\Omega} \tag{7}$$

where $\Delta V_i = V_i - V_{i+1}$ is the volume change in a $\Delta t_i = t_{i+1} - t_i$ time interval. The hydrodynamic resistance of a rectangular channel with close to unity width to height ratio ($w/\hat{h} \cong 1$) under laminar flow conditions is:[13]

$$W=\frac{12\mu L}{w\hat{h}^3}\left[1-\frac{\hat{h}}{w}\left(\frac{192}{\pi^5}\right)\sum_{n=1,3,5}^{N=11}\frac{1}{n^5}\tanh\left(\frac{n\pi w}{2\hat{h}}\right)\right]^{-1} \tag{8}$$

where μ is the viscosity of the fluid, L is the length of the channel, w is the width of the channel, and $\hat{h}$ is the height of the channel. However, the model does not include energy exchanges that are small or transient, i.e., the time and work to accelerate the fluid from static condition to steady state flow with Poiseuille profile are neglected.

The changes in the sample volume and flow rate with time have been calculated by using a Matlab program. The volume of the droplet sinking into the entry port of the micro-channel has been computed for its initial value ($t_i=t_0$ and $h_i=h_{i,max}$) and following each 2 μm incremental change in the height of its apex (h_i). The value of n in Eq. 8 was set to 11. With N=11 the calculated hydrodynamic resistance has less than 0.001% error compared to its actual value (n=∞).

Experimental

The micro-fluidic systems for this study were made with conventional techniques for soft lithography by casting Sylgard 184 (Dow Corning, MI) poly-dimethylsiloxane (PDMS) on a silicon master.[14] After curing the PDMS replica of the master, its surface was treated in a 300 mTorr air plasma using PDC-32G plasma cleaner (Harrick Scientific, Pleasantville, NY) in combination with a Robinair model 15600 vacuum pump (SPX Corp. Montpelier, OH) and then bound to a flat, simultaneously treated PDMS surface to form the channel. This plasma treatment procedure increases the hydrophilicity of the PDMS-based micro-channels. However, this induced hydrophilicity is gradually lost. The rate at which the loss occurs depends on the environment in which the plasma-treated PDMS is stored. An air plasma treated

PDMS retains its hydrophilic properties over a one month period when kept in contact with deionized water.[15]

The passive flow micro-fluidic system shown in Fig. 1 has been tested in horizontal position. It has cylindrical entry and exit ports that are connected by a rectangular micro-channel. The nominal dimensions of the micro-channels were 5.0 or 10.0 mm long; 192 μm wide; and 96 μm high. The actual dimensions were measured with a Nikon Eclipse E600 (Nikon, Japan) optical microscope. The approximately 1 mm deep, cylindrical entry and exit ports (wells), perpendicular to the rectangular micro-channel, were created by punching the PDMS slab with a sharpened glass pipette. Inspection with a microscope showed that the punched edges were free of burrs. The diameter of the entry port was 1.8 mm; 2.5 and 3.3 mm diameter exit ports were utilized in the different experiments.

Air bubbles in the micro-channel induce unexpected resistance in the flow-through system.[16] To prevent the appearance of trapped air bubbles in the micro-channel and the connected wells the micro-fluidic manifolds were first filled with methanol, which was subsequently replaced with deionized water. Deionized water (18.2 Mohm resistivity) provided by a Milli Q Gradient A-10 water purification system (Millipore, MA) was used in all experiments.

Once filled with deionized water the micro-channel is ready for passive pumping. In our protocol, first the volume of the reservoir droplet is set by adjusting its height to the required value (approximately 0.4 mm, representing ~1.1 or ~2.3 μL reservoir volumes for wells with 2.5 or 3.3 mm diameter, respectively). Next, a 2.5 μL sample droplet is placed onto the entry port of the device. With placing the sample droplet onto the entry port of the device the flow begins and the droplet's image is captured. Then images of the sample droplet are captured every second for a minimum of 60 seconds. The pumped sample volume is calculated from the acquired images. A VCA Optima Surface Analysis System (Advanced Surface Technology, Billerica, MA) with 7.3 μm/pixel resolution has been used for imaging the sample and reservoir droplets.

Parameters in our model calculations were the volumes of the sample and reservoir droplets, the channel geometry, and the viscosity (1 cP), density (0.998 g/cm^3), and surface tension (72.88 dyne/cm) of pure water[12]. The validity of our model, especially its assumptions, has been tested in four sets of experiments (A, B, C, and D) that were designed to study the effect of the (i) hydrodynamic resistance, (ii) reservoir diameter and (iii) material properties of the channel on the induced flow rate. The volumes, heights and radii of the sample and reservoir droplets utilized in these four sets of experiments are summarized in Table 1, which also contains the pressure differences of Eq. 5 that reflect the experimental conditions at time zero, the time instant when passive pumping process was initiated. In the first set of experiments, (row A), a 1.8 mm diameter sample port was connected to a 2.5 mm diameter reservoir port via a 5.0 mm long rectangular channel. In the second set of experiments, (row B), the dimensions of the sample and reservoir ports were the same as in experiments shown in row (A) of Table 1 but the channel length has been doubled from 5.0 to 10.0 mm to show the effect of the hydrodynamic resistance on the induced flow rate. In the third set of experiments, (row C), a 1.8 mm diameter sample port was connected to a 3.3 mm diameter reservoir port via a 5.0 mm long rectangular channel. So, by comparing the results of experiments shown in rows (A) and (C) the effect of increased reservoir port diameter on ΔP_R and the induced flow rate could be demonstrated. Finally, in the fourth set of experiments, (row D), the dimensions of the micro-fluidic channel were the same as in experiments shown in row (A) of Table 1 but the entry port of the device was made somewhat hydrophilic through air plasma treatment. The differences in the induced flow rates in experiments summarized by data in rows (A) and (D) are related to the differences in the surface properties and geometries of the two micro-fluidic devices.

The pressure differences in Table 1 were calculated to show the different results by using the classical (Eq. 4a) or the modified (Eq. 4b) Young-Laplace equation for estimating the passive pump induced flow rate in micro-fluidic channels. The hydrodynamic resistances of a 5.0 and a 10.0 mm long channel, used in this work, were determined as $5.15 \cdot 10^6$ and $10.3 \cdot 10^6$ dyne·sec/cm^5, respectively. The hydrodynamic resistances of the wells are six orders of magnitude less than that of the micro-channels, hence their contributions were neglected.

Results and Discussion

On hydrophobic surfaces, water molecules tend to aggregate, the contact angle ϕ is larger than 90°, and $a < h$. In contrast, on hydrophilic surfaces water droplets tend to spread, ϕ is smaller than 90°, and $a > h$. The contact angles measured on the surfaces of the micro-fluidic devices used in this work were 112 ± 4 degrees (hydrophobic) and 86 ± 1 degrees (somewhat hydrophilic). The half chord lengths of 2.5 μL volume water droplets, placed over the entry ports of the hydrophobic devices (a = 1.0 mm), were about the same size as the radii of the wells (r=0.95 mm). In contrast, on the slightly hydrophilic surfaces the sample droplets spread outside the wells, i.e., the half chord lengths of 2.5 μL volume water droplets (a = 1.16 mm), were larger than the radiuses of the wells (r=0.98 mm). However, the cord length of the droplets on both the hydrophobic and hydrophilic PDMS surfaces remained nearly constant during the entire pumping process.

The flow rate in a passive flow driven micro-fluidic device depends on the overall pressure difference (ΔP_{total}) between the sample and reservoir ports of the micro-channel and the hydrodynamic resistance (Ω) of the micro-channel (Eq. 7). The total pressure difference (Eq. 5) is governed by the pressure differences generated at the interfaces of the sample (ΔP_S) and reservoir (ΔP_R) droplets and the hydrostatic pressure difference (ΔP_H). All three pressure differences change in time. The magnitude (Table 1) and time dependence (Fig. 3) of the individual pressure differences determine the time dependence of the passive pump driven flow rate in the micro-channel. The terms in Eq. 5 can be calculated by Eqs. 4a or 4b (ΔP_S and ΔP_R) and Eq. 6 (ΔP_H). In this work, the advantages of using modified Young-Laplace equation (Eq. 4b) instead of its classical form (Eq. 4a) for calculating ΔP_S and ΔP_R and evaluating the passive pump induced flow rate in micro-fluidic channels is assessed in four sets of experiments. As we show in Table 1, the relative contribution of the individual pressure differences to ΔP_{total} and the absolute values of ΔP_{total} are strongly influenced by the experimental conditions, i.e., the volume of the sample and reservoir droplets and the dimensions of the sample and reservoir wells. Similarly, the difference in the ΔP_{total} values calculated with Eq. 4a and 4b depend on the experimental conditions. The differences between the values calculated with Eq. 4a or 4b were the largest (around 20 %) in experiments of row (A) in Table 1. The time dependences of the individual pressure differences and ΔP_{total} are shown in Fig. 3 for the experimental conditions summarized in row (A) in Table 1. From the data in Table 1 and Fig. 3 it is obvious that the pressure difference generated by the surface tension at the reservoir droplet (ΔP_R) and the hydrostatic pressure difference (ΔP_H) are significant and cannot be neglected when the overall pressure difference (ΔP_{tot}) is determined. The error in ΔP_{total} can be greater than 50% when the contributions of ΔP_R and ΔP_H are disregarded in the calculations. Likewise, ΔP_R and ΔP_H should not be assumed constant. As shown in Fig. 3, the time dependent changes in ΔP_R and ΔP_H significantly influence the time course of ΔP_{total}.

In Figs. 4a through 4d the sample droplet volumes assessed from captured images and calculated by using different models are compared as function of time. The experimental conditions utilized in recording the data of Figs. 4a through 4d correspond to the experimental conditions in rows (A) through (D) in Table 1. In the figures the circles represent the volumes calculated from the captured images of the sinking droplets. The solid lines represent droplet

volumes calculated with our computational model by utilizing Eq. 4a or Eq. 4b in combination with Eq. 5. Finally, the red diamonds represent computed volumes based on the model of Berthier's et. al.[11] The images in Fig. 4e are shown to prove the validity of the assumption of constant chord lengths for the sample droplet in our computational model. These images were captured at t=0, 8 and 35 s after the passive flow in the micro-fluidic device has been initiated. Similar to Fig. 4e, in all of our experiments the half chord lengths of the sample droplets remained practically constant during the entire pumping process or its decrease remained always below 1 %.

A striking aspect of Fig. 4 is the difference between the quality of the description of the experimental data with the computational models and with the analytical description obtained by Berthier et. al.[11] This difference is assumed to be related to differences in the experimental conditions. In the work of Berthier et. al. the radii of sample and reservoir ports were much smaller than the half chord length of the droplets and the volume of the reservoir droplet was much larger than that of the sample droplet. Due to the large difference in the volumes of the sample and reservoir droplets Berthier assumed that changes in ΔP_R can be neglected. For the same reason, changes in the hydrostatic pressure differences (ΔP_H) caused by the height difference between sample and reservoir droplets were ignored. These assumptions are not met for the experimental conditions used in this work (see Table 1 and Fig. 4), but the conditions of the experiments are suited to practical lab-on-a-chip devices. Indeed, neglecting changes in ΔP_R and ignoring changes in ΔP_H could have a significant influence on ΔP_{tot} and the calculated flow rates even in systems with large reservoir droplet volumes (e.g. V_S=2.5 μL and V_R=20.0 μL). Large reservoir droplets were avoided in this work because above 10 μL the shapes notably diverged from the ideal spherical shape, and this shape could not be taken into account in our computational model.

In contrast to Berthier's model[11] our computational approach provides a reasonable match between measured and calculated volumes. However, in three of the four examples discussed in this paper (Figs. 4a, b, and c corresponding to rows (A), (B) and (C) in Table 1) the computed volumes decreased somewhat faster than the experimentally measured ones, i.e., the actual flow rates were smaller than predicted by the model. The reasons for the differences between the computed and measured rate of change in the sample volume (Figs. 4a, b, and c) are not clear. The inaccuracies in estimating the $dh_{i,j}$ values (Fig. 2d) with a cosine function as discussed in supplementary material (Eq. S1) could be an explanation. Hardly visible air bubbles trapped in micro-channel may have increased the hydrodynamic resistance of the system, which is a factor that was not considered in our model. Similarly, a slight slope of the channel was not considered in our model although the perfect horizontal placement of the channel could not be unambiguously assured in our protocol. Small slopes can slow or enhance the experimentally recorded flow rates. Finally, evaporation related losses in the sample and reservoir droplet volumes can play a role in the measured flow rates. This factor was neglected in this work because in control experiments the mass losses from 2.5 μL volume deionized water droplets were always below 5% in the time frame of our experiments.

As shown in Table 1 the various experimental conditions generate different pressure differences which in turn produce different flow rates in the micro-fluidic manifolds (Figures 4 and 5). For example, a 2.5 μL volume sample droplet generated 150 nL/s initial flow rate (Fig. 5a) in a 5.0 mm long micro-channel channel with a 2.5 mm diameter reservoir port. The influence of the channel resistance on the generated flow rate can be seen by comparing the flow rates generated in a 5.0 and 10.0 mm long flow channels (Figures 5a and 5b). In agreement with the expectations, the same 2.5 μL volume sample droplet generated about half of the initial flow rate in the 10.0 mm (85 nL/s) channel than in the 5.0 mm (150 nL/s) long one. The influence of the reservoir diameter on the induced flow rate can be assessed by comparing Figures 5a and 5c. Increasing the diameter of the reservoir well decreases ΔP_R and increases

ΔP_{tot}. When the diameter of the reservoir well was increased from 2.5 to 3.3 mm a 2.5 μL sample droplet generated 196 nL/s initial flow rate (Fig. 5c) instead of 150 nL/s (Fig. 5a) in the same length of channel. The effect of the surface properties of the micro-fluidic manifold on the generated flow rate can be evaluated by comparing the Figures 5a and 5d. Over hydrophilic entry ports, the sample droplets have bigger radii which mean decreased ΔP_S compared to hydrophobic entry ports. Consequently the induced flow rates in such systems are expected to be smaller. Indeed, when a 2.5 μL sample droplets were placed over the hydrophilic entry port of a 5.0 mm long channel they induced only 121 nL/s initial flow rate (Figure 5d).

Similar to the ΔP_{tot} vs. time curve (Fig. 3), the computed flow rate vs. time curves in Fig. 5a, b and c have three well defined phases with transition times that are strongly correlated with the shape changes in the "pumping" (sample) droplet (pseudo-concentric descent). These shape changes can be characterized as changes in the radius of the droplet. The first transition time appears at the curves when the pumping droplet has a minimum radius and ΔP_S peaks (around 8s in Fig. 3). After the first transition phase, the radius of the droplet gradually increases, with simultaneous gradual decrease in ΔP_S, ΔP_{tot} and induced flow rate. The flow stops when ΔP_{tot} drops to zero (second transition time around 25s in Fig. 3), i.e., the system reaches equilibrium. On the surface of a hydrophilic channel (Fig. 5d) the radius of the sample droplet continuously increases as the droplet sinks into the sample well (pseudo-concentric descent with increasing radius as shown in Fig. 2d). Consequently, ΔP_S, ΔP_{tot} and the induced flow rate continuously decreases without an apparent transition time.

Based on the data summarized in Table 1 and Figures 4 and 5, it is clear that the use of the more complex computational approach (Eq. 4b instead of Eq. 4a) is not essential for all experimental conditions. Indeed, in two of the four sets of experiments (Figs. 4c and 4d), the curves calculated with the different models were indistinguishable. The differences between the two computational approaches (Eq. 4a and 4b) become more noticeable by plotting the calculated flow rates vs. time (Fig. 5). Although the more complex computational model seems to provide somewhat better fits, its advantages could not be proved unambiguously due to the relatively large standard deviation of the experimental data. The large standard deviations of the experimental data points in Fig. 5 are the consequences of the limited resolution of the digital camera utilized to capture images of the sample droplets sinking into the input port of the device, and the non-linear equation (Eq. 2) used to calculate the droplet volumes from the captured images. A single pixel difference in the digital camera reading can easily change the calculated flow rate by 50%. For example, the calculated flow rate of the data point marked with the filled circle (5.5 s, 46 nL/s) in Fig. 5b would increase from 46 nL/s to 69 nL/s when the reading of the height of the sinking droplet were changed from 155 to 156 pixels.

Conclusion

Passive pumps can provide low flow rates with good reproducibility. The induced flow rates can be controlled by the material (hydrophobic vs. hydrophilic) and geometrical properties of the channel (shape, height, length and slant), the sample and reservoir wells (diameter) and the sample and reservoir droplets (volume, surface tension, density and viscosity). A computational model has been derived to describe the time dependent flow rate in a passive pump driven micro-fluidic system. The effects of the experimental parameters on the calculated flow are demonstrated. The results from computational model are consistent with experimental results measured in micro-fluidic systems with different channel length (5.0 and 10.0 mm), reservoir well diameter (2.5 and 3.3 mm) and surface properties (hydrophobic or hydrophilic). The mathematical model is expected to help designing passive flow driven micro-fluidic systems with required flow conditions.

Supplementary Material

Refer to Web version on PubMed Central for supplementary material.

Acknowledgments

This work has been supported by the NIH/NHLBI grant # 1 RO1 HL079147-01.

References

1. Andersson H, van der Wijngaart W, Nilsson P, Enoksson P, Stemme G. Sensors and Actuators, B 2001;72:259–265.
2. Bohm S, Olthuis W, Bergveld P. Sensors and Actuators, A 1999;77:223–228.
3. Gallardo BS, Gupta VK, Eagerton FD, Jong LI, Craig VS, Shah RR, ANL. Science 1999;283:57–60. [PubMed: 9872739]
4. Good B, Bowman C, Davis R. Journal of Coliod and Interface Science 2004;14:239–249.
5. Khoo M, Liu C. Sensors and Actuators, A 2001;89:259–266.
6. Kirby BJ, Hasselbrink EF. Electrophoresis 2004;25:187–202. [PubMed: 14743473]
7. Vestad T, Marr DWM, Oakey J. Journal of Micromechanics and Microengineering 2004;14:1503–1506.
8. Handique K, Burke DT, Mastrangelo CH, Burns MA. Anal Chem 2000;72:4100–4109.
9. Burns MA, Johnson BN, Brahmasandra SN, Handique K, Webster JR, Krishnan M, Sammarco TS, Man PM, Jones D, Heldsinger D, Mastrangelo CH, Burke DT. Science 1998;282:484–487. [PubMed: 9774277]
10. Walker GM, Beebe DJ. Lab on a Chip 2002;2:131–134. [PubMed: 15100822]
11. Berthier E, Beebe D. Lab on a Chip 2007;7:1475–1478. [PubMed: 17960274]
12. Adamson, AW. A Textbook of Physical Chemistry. Academic Press; New York: 1979.
13. White, F. Viscous Fluid Flow. McGraw-Hill; Rhode Island: 2006.
14. Sia SK, Whitesides GM. Electrophoresis 2003;24:3563–3576. [PubMed: 14613181]
15. Chen IJ, Lindner E. Langmuir 2007;23:3118–3122. [PubMed: 17279784]
16. Stone HA, Stroock AD, Ajdari A. Annual Review of Fluidic Mechanics 2004;36:381–411.

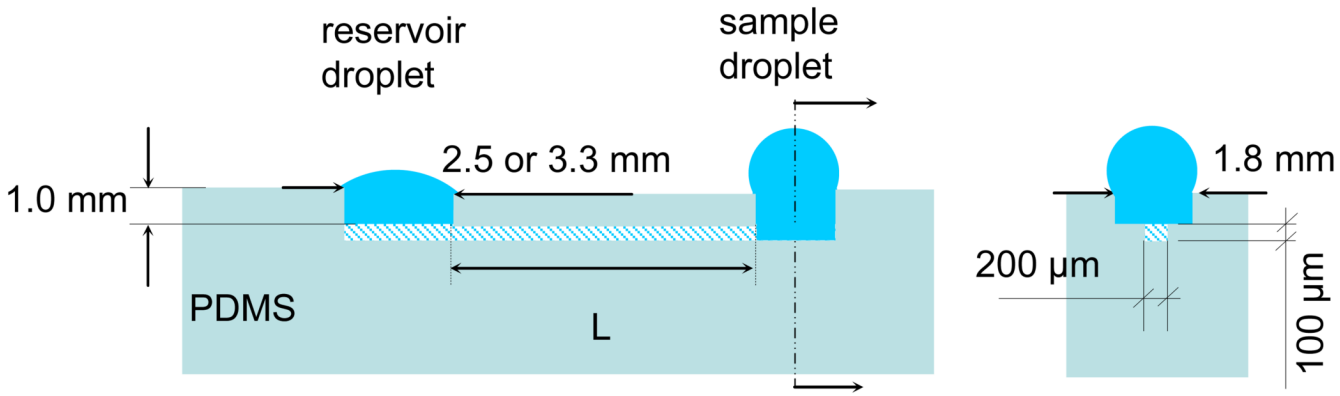

Fig. 1.
Front and end cross sectional views of the polydimethylsiloxane (PDMS)-based micro-fluidic system used in passive pumping experiments.

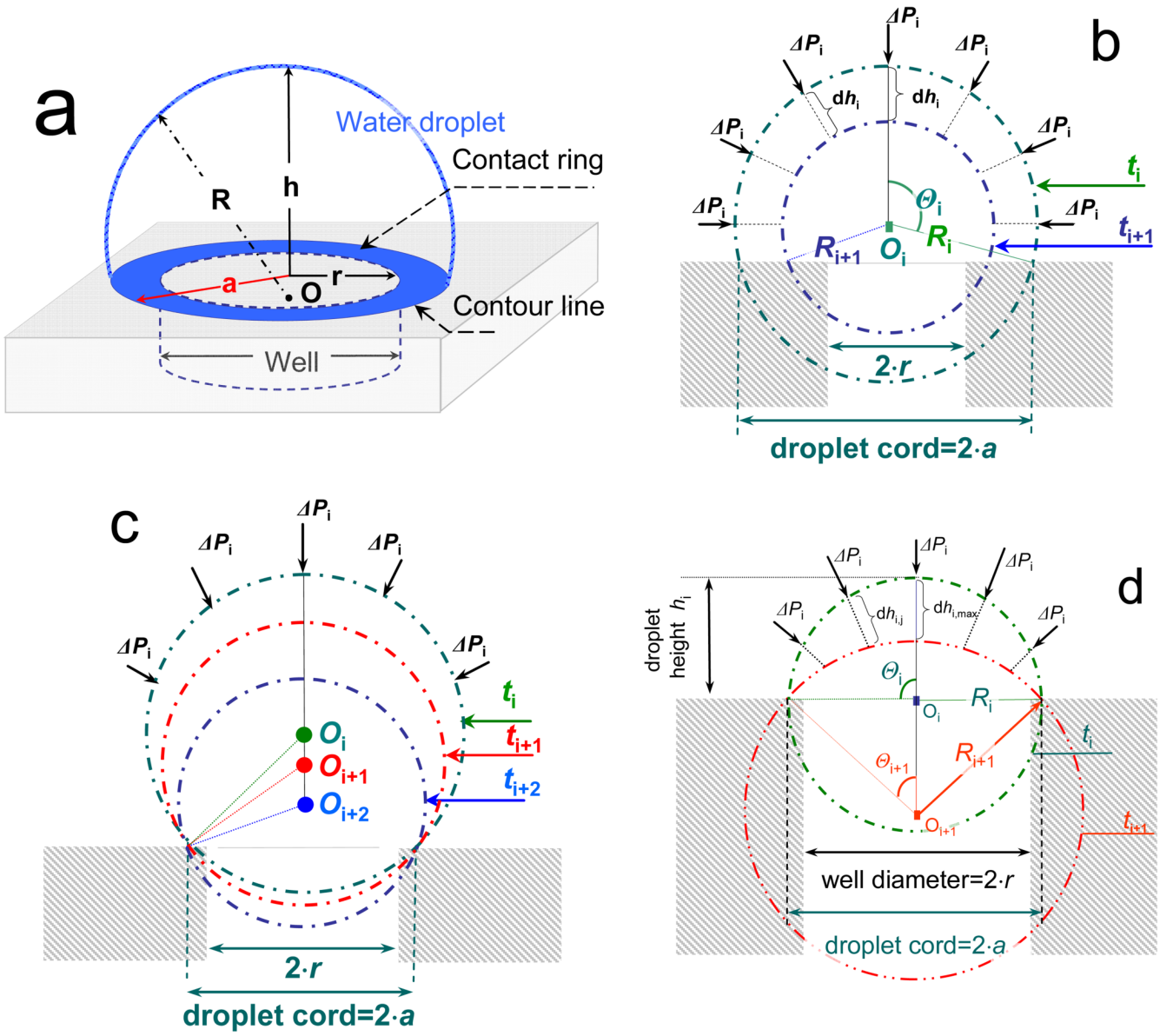

Fig. 2.

Schematic view of a droplet placed over a cylindrical entry port of a micro-fluidic device (a) and cross sectional snapshots of droplets sinking into cylindrical entry ports with different descent patterns: (b) concentric with decreasing cord length, (c) pseudo-concentric with fixed cord length, decreasing *R*, and descending center, (d) pseudo-concentric with fixed cord length, increasing *R*, and descending center. Consecutive time instances are labeled as t_i, t_{i+1}, and t_{i+2}, *r* is the radius of the cylindrical entry port, *a* is the half chord length of the droplet, *h* is the height of the droplet above the surface of the micro-fluidic manifold, *R* is the radius of the droplet, *O* is the center of the droplet, Θ is the half-angle of the arc, ΔP_i is the pressure difference measured from inside to outside, dh_i, and $dh_{i,j}$ are distances the individual points of the air/water interface descent in a time interval Δt. The subscripts of *O*, *R*, and Θ correspond to the time instances t_i, t_{i+1} and t_{i+2}.

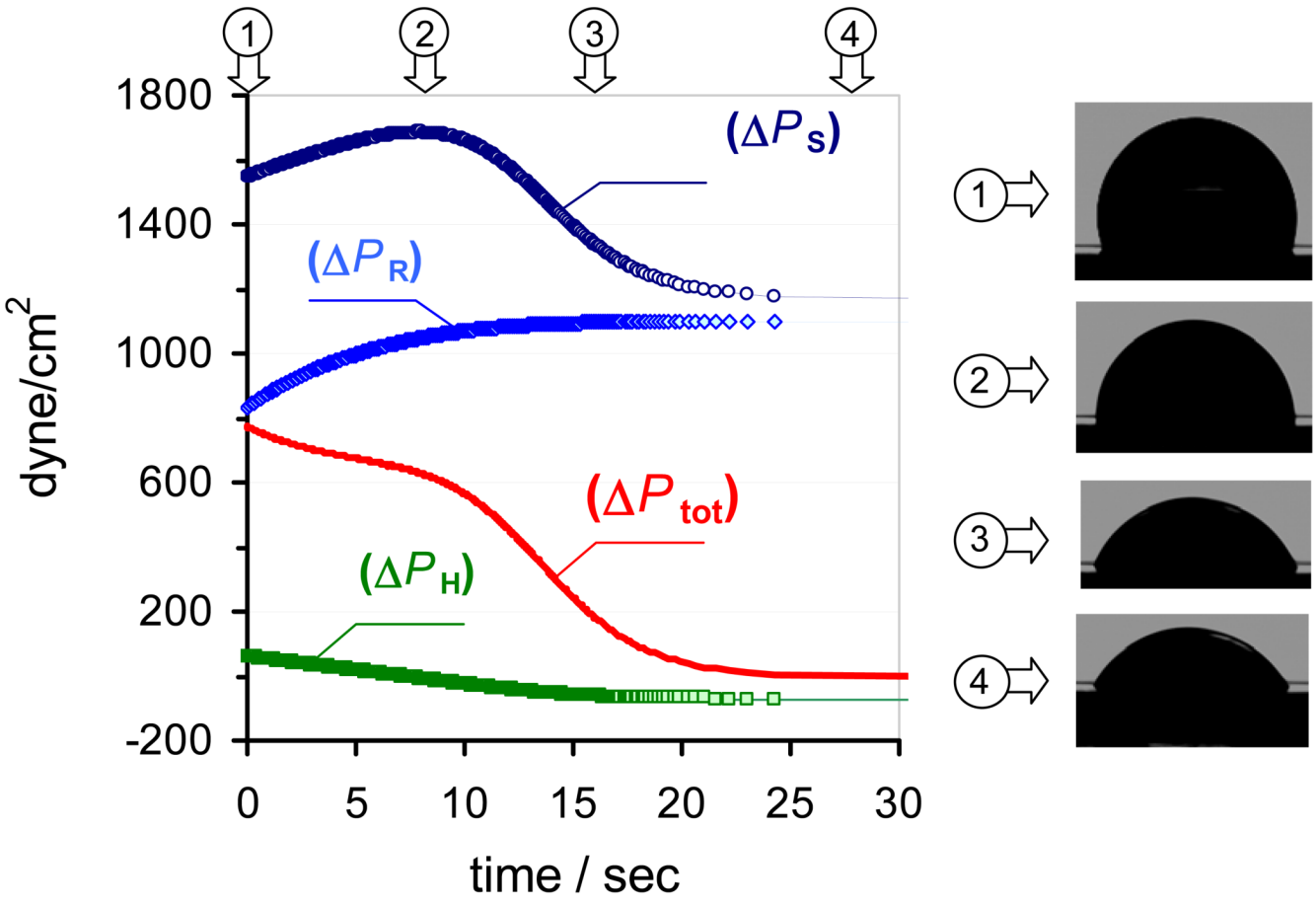

Fig. 3.

The time dependence of the individual pressure differences (Eqs. 4b and 6) and the total pressure difference (Eq. 5) in a passive flow driven micro-fluidic system. The experimental conditions are in row (A) in Table 1. ΔP_S and ΔP_R are pressure differences generated at the interfaces of the sample and reservoir droplets, ΔP_H is the hydrostatic pressure difference related to differences in the height of the sample and reservoir droplets and ΔP_{tot} is the total pressure difference calculated by Eq. 5. The images of the droplets correspond to time instances marked on the top of the figure.

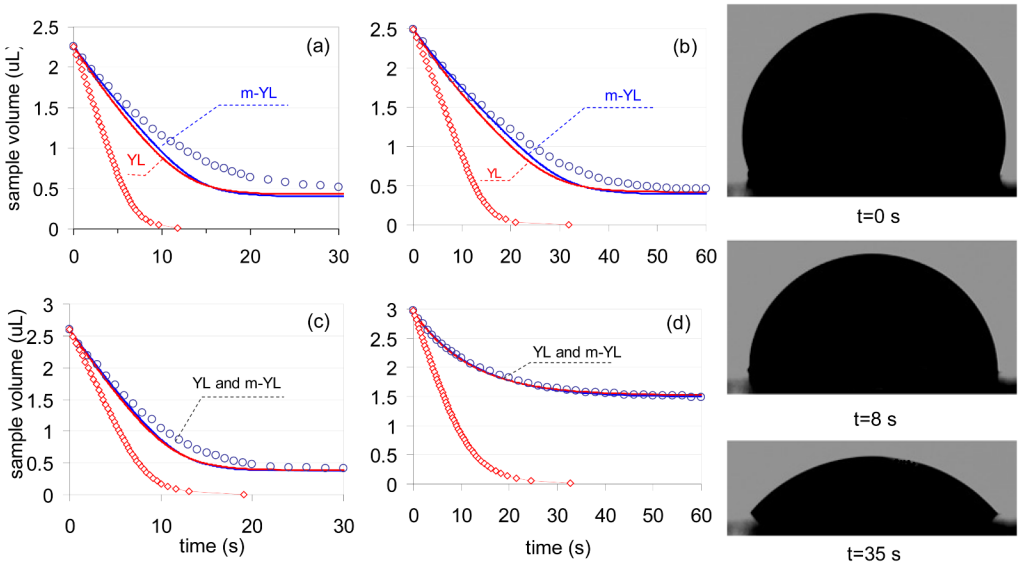

Fig. 4.

Comparison of the experimentally measured (○) and computed sample droplet volumes in four sets of experiments. The red and blue solid lines were calculated by utilizing the traditional Young-Laplace equation (Eq. 4a, labeled as YL) or its more complex form (Eq. 4b labeled as m-YL) in combination with Eq. 5, respectively. The red diamonds represent the computed results based on Berthier's model.[11] (a) 5.0 mm hydrophobic PDMS channel with 2.5 mm diameter reservoir port (b) 10.0 mm hydrophobic PDMS channel with 2.5 mm diameter reservoir port. (c) 5.0 mm hydrophobic PDMS channel with 3.3 mm reservoir port (d) 5.0 mm hydrophilic PDMS channel with 2.5 mm diameter reservoir port. (e) Images of sample droplets captured during the experiment shown in 4a.

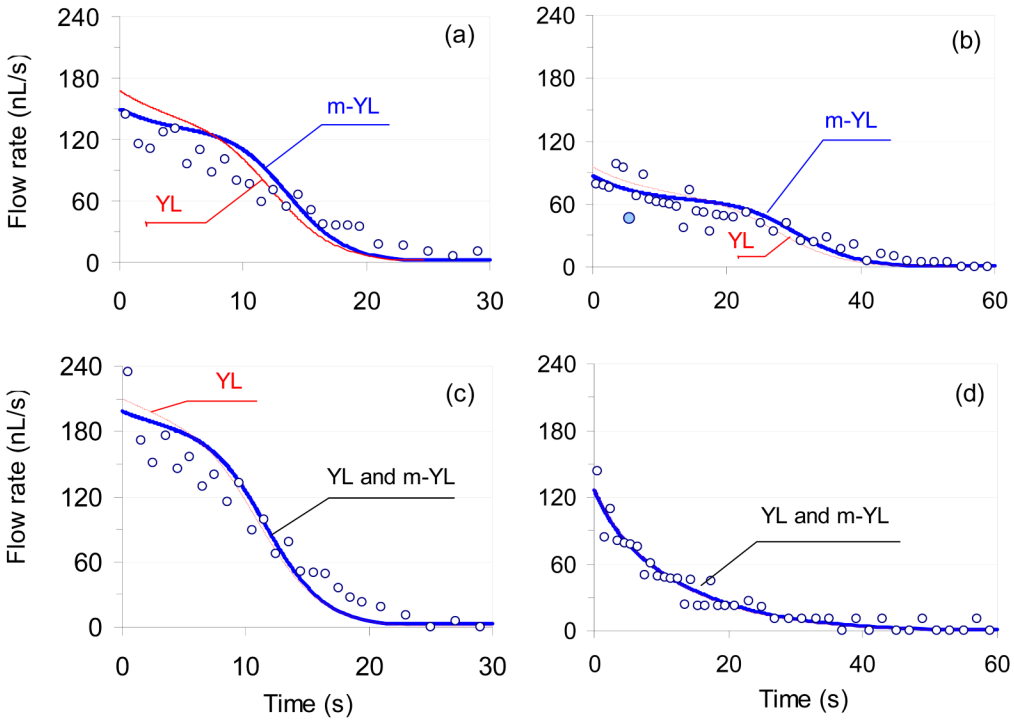

Fig. 5.

Experimentally measured (○) and computed volumetric flow rates in four sets of experiments. The red and blue solid lines were computed by utilizing Eq. 4a and 4b in combination with Eq. 5 and 7, and are marked as (YL) or (m-YL), respectively. When the lines ran on the same path they are labeled as (YL and m-YL). The experimental conditions were the same as in Fig. 4 and are summarized in Table 1.

Table 1

Experimental conditions and corresponding pressure differences at time zero in passive pump driven micro-fluidic systems discussed in this paper.

Exp. #	channel length (mm)	droplet volume (μL)		droplet height (mm)		droplet radius (mm)		pressure differences derived from Eqs. 4a[†] and 4b[‡] (dyne/cm^2)			
		V_S	V_R	h_S	h_R	R_S	R_R	ΔP_S	ΔP_R	ΔP_H	ΔP_{total}
A	5.0	2.26	1.64	1.2	0.6	0.91	1.82	*1602* **1493**	*801* **832**	59	*860* **720**
B	10	2.49	1.12	1.3	0.4	0.92	2.13	*1584* **1513**	*684* **700**	88	*988* **901**
C	5.0	2.60	2.34	1.2	0.5	0.97	3.01	*1503* **1457**	*454* **503**	69	*1118* **1023**
D	5.0	2.97	1.09	1.1	0.4	1.17	2.21	*1246* **1259**	*660* **671**	69	*655* **657**

[†]Printed *italic*.

[‡]Printed **bold**.